PAPER

Check for updates

Plasmonic nanoparticles boost low-current perovskite LEDs governed by photon recycling effects

Jaime Bueno, [ID] [a] Alberto Jiménez-Solano, [ID] [b] Miguel Anaya [ID] *[c] and Sol Carretero-Palacios [ID] *[a]

Perovskite light-emitting diodes (PeLEDs) have emerged as a promising technology for next-generation display and lighting applications, thanks to their remarkable colour purity, tunability, and ease of fabrication. In this work, we explore the incorporation of plasmonic spherical nanoparticles (NPs) directly embedded into the green-emitting $CsPbBr_3$ perovskite layer in a PeLED as a strategy to enhance both its optical and electrical properties. We find that plasmonic effects directly boost spontaneous emission while also influencing charge carrier recombination dynamics. We present a rigorous theoretical electro-optical analysis to systematically investigate the impact of NP metal, size, and concentration on device performance, with particular emphasis on the role of photon recycling (PR). Our results demonstrate that embedding carefully designed silver (Ag) NPs, selected through rigorous theoretical modelling, into PeLEDs leads to enhanced device performance across a wide range of operating currents. Notably, we observe a 4-fold improvement in external quantum efficiency (EQE) at injection currents as low as 0.02 mA cm^{-2}, and a 2-fold enhancement at 0.2 mA cm^{-2}, attributed to increased radiative recombination. Furthermore, results suggest improved efficiency retention at higher injection levels, pointing to reduced current roll-off limitations and extended high-brightness operation. Additionally, PR plays a crucial role in mitigating optical losses and improving outcoupling efficiency, especially in plasmonic-enhanced systems, where scattering effects increase the prevalence of trapping states. These findings open up exciting possibilities for devices requiring energy-efficient, compact, and high-performance light sources, such as portable electronics and low-power displays.

[a]Instituto de Ciencia de Materiales de Madrid, ICMM-CSIC, C/Sor Juana Inés de la Cruz, 3, Madrid, 28049, Spain. E-mail: sol.carretero@csic.es

[b]Departamento de Física, Universidad de Córdoba, Edificio Einstein (C2), Campus de Rabanales, Córdoba, 14071, Spain

[c]Instituto de Ciencia de Materiales de Sevilla, Universidad de Sevilla−CSIC, Calle Américo Vespucio 49, Sevilla 41092, Spain. E-mail: anaya@us.es

Introduction

Light-emitting diodes (LEDs) have been established as the dominant platform for solid-state lighting and optical communication. Their versatility has enabled their integration across a broad range of applications, including both indoor and outdoor illumination, displays, visible light communication or LiFi, biomedical devices, and wearable gadgets.[1–8] Nevertheless, LEDs equipped with specialized features are further required to address all growing demands, such as energy efficiency, high brightness, colour purity, stability, directionality, and stretchable or flexible devices.[9–11] Particularly, with the rise of Internet of Things (IoT) devices,[12] low-power operation has become important, yet it remains challenging due to the inherent losses from non-radiative recombination at low injected currents.[13,14]

Additionally, high-power LEDs are essential for applications requiring high brightness, such as outdoor displays, large-scale signage and long-range communications, where managing power dissipation and mitigating roll-off effects are crucial for maintaining performance and longevity.[15–19]

Metal halide perovskites have gained significant attention in the field of light emission due to their outstanding optoelectronic properties, including colour purity, high photo-luminescence quantum yield, long carrier diffusion lengths, tuneable bandgap, facile solution processability and photon recycling (PR) capabilities.[20–23] Recent reports have demonstrated external quantum efficiencies (EQE) exceeding 30% for near-infrared and green-emitting perovskite light-emitting diodes (PeLEDs),[24,25] over 25% for red,[26] and over 18% for blue,[27] marking significant advancements in their performance across different spectral regions, paving the way for the commercialization of both next generation efficient lighting devices and flat-panel displays.[28–31] The optimization of the materials involved in the whole PeLED architecture plays a crucial role in enhancing charge balanced transport, light generation, and stability.[29,32,33] However, aside from the intrinsic properties of the device materials, there are other

factors associated with the light–matter interactions across the system that limit its potential efficiency. Due to the high refractive indices contrast between both the perovskite emitting layer (EML), and the rest of layers composing the device (*i.e.*, electron transport layer (ETL), hole transport layer (HTL), and substrate), and the far-field medium where light is radiated (generally air), waveguide modes are formed because of total internal reflections, resulting in suboptimal light extraction.[34,35] In addition, the requirement for specific emission properties (*i.e.*, colour purity, directionality, integrability, and low- and high-power operation) across various applications demands exquisite control over the behaviour of light within the devices.

In this context, photonic structures for improved light management in PeLEDs have been proposed.[4,11] Optimized functional layer thicknesses,[36–38] controlled anisotropy of the EML,[39,40] photonic crystals,[41–44] and modifications of planar interfaces, such as nanophotonic substrates,[45,46] nanopatterned structures,[47–50] domical textures[51] or perovskite nanoplatelets,[52] have been extensively explored as promising strategies for improved light outcoupling. Other nanophotonic approaches managing surface plasmons (SPs) have also been studied to reduce the optical energy lost in surface plasmon polaritons modes at metallic–dielectric interfaces, and to accelerate spontaneous emission rate at the device,[53,54] featuring improved EQEs. For instance, the use of Tamm-plasmon resonances at metallic–photonic crystal interfaces have been employed for spectral and directional emission control.[55] Coaxial hetero-structured PeLEDs combining gold (Au) nanoparticles (NPs) and *n*-ZnO nanowires as carrier injectors have also been considered, simultaneously addressing emission efficiency and stability issues.[56] Silver (Ag) nanorods have been embedded in a barrier layer placed between the perovskite EML and the HTL,[57] and Ag and Au NPs have been included inside the HTL or ETL.[58–62] However, in contrast to other more matured perovskite-based optoelectronic devices such as single-junction and tandem perovskite solar cells,[53,63–65] the use of metallic NPs directly integrated into the EML layer in PeLEDs aimed at leveraging local density of optical states (LDOS) enhancement, remains largely unexplored from a rigorous theoretical stand-point. In addition, perovskite semiconductors exhibit a low Stokes shift, enabling PR through re-absorption of emitted photons.[66–70] When combined with optimized designs and highly radiative materials, PR enhances optical outcoupling by redirecting originally trapped photons, potentially contributing up to a 70% of the EQE in state-of-art devices.[71,72]

Herein, we propose the use of metallic NPs supporting localized surface plasmonic resonances (LSPRs) directly embedded into the EML for a surgically management of both optical and electrical behaviour in the system. In contrast to other strategies aimed at improving PeLED efficiency, such as the use of photonic crystals or the optimization of emitting layer thickness, our approach leveraging plasmonic NPs offers a promising pathway to not only enhance spontaneous emission by increasing the LDOS but also extend the operational range of PeLEDs across low and high current injection regimes. We first present a three-dimensional (3D) Finite-Difference Time-Domain (FDTD) model that enables the inclusion of

volumetric metallic nanostructures within the EML. Simulations reveal that embedding spherical Ag NPs with a 15 nm radius in a 50 nm thin $CsPbBr_3$ film can lead to an 8-fold enhancement in dipolar emission to the far-field compared to a NP-free reference. Additionally, in PeLEDs with a 150 nm thick EML, the angular emission distribution can be effectively tuned *via* NP size, with 50 nm and 20 nm Ag NPs promoting forward directed or diffuse light output, respectively. A more realistic plasmonic PeLED model is then evaluated, incorporating the carrier-density-dependent quantum yield (QY) and, for the first time reported in this context, PR effects in this complex 3D system. The integration of metal NPs is shown to enhance the effective QY, lowering radiative threshold and enabling efficient low power operation. This not only reduces temperature-induced losses and material degradation but also increases tolerance to defect states by masking the impact of trap-assisted recombination. Similarly, a delayed onset of the Auger recombination regime is observed, effectively mitigating the current-efficiency roll-off, and enabling highly bright and stable PeLED operation.[15–18]

Theoretical modelling

In LEDs, the EQE is defined as the ratio between the number of photons extracted from the device and the number of injected charges. It can be expressed by the product of several efficiencies that characterize different processes occurring in the device, from the injection of charges to the emission of photons into the far field, as represented in eqn (1),

$$EQE = \gamma \cdot \Phi \cdot \eta \quad (1)$$

where γ represents the electrical efficiency of the system prior to any photon emission. It involves two factors, usually denoted in the literature as $f_{balance}$ and f_{e-h}, representing the charge injection balance, and the likelihood of forming a correlated hole–electron pair or exciton from each pair of injected carriers, respectively. For simplicity, in this work, γ will be ideally assumed to be equal to unity since our discussion will be strictly centred in recombination processes and optical behaviour. In the above expression, Φ denotes the QY, which expresses the ratio of radiatively recombined excitons to all the recombination processes involved, and can be expressed in terms of the spontaneous radiative (Γ_r) and non-radiative (Γ_{nr}) decay rates as $\Phi = \Gamma_r/(\Gamma_r + \Gamma_{nr})$. Finally, η denotes the outcoupling efficiency, which sets the fraction of photons that escapes the whole device from those that were generated.[35,73]

Fermi's golden rule, commonly used to describe interband radiative recombination in direct bandgap semiconductors, reveals that the spontaneous emission rate depends on the emitter's environment through its relation to the LDOS.[74–76] The enhancement of Γ_r of a material embedded in a given system, relative to the intrinsic rate of an infinite homogeneous medium ($\Gamma_{r,o}$), is known as the Purcell factor (F).[77,78] As a result, the actual emission rate within the system can be expressed as $\Gamma_r = F \cdot \Gamma_{r,o}$. Incorporating this relationship into the expression

for the QY, allows us to define the effective QY of the system, Φ, as a function of the intrinsic QY of the material, Φ_o:[79]

$$\Phi = \frac{F \cdot \Gamma_{r,o}}{F \cdot \Gamma_{r,o} + \Gamma_{nr}} = \frac{F \cdot \Phi_o}{1 + (F - 1)\Phi_o} \quad (2)$$

Note that the theoretical intrinsic quantum yield, Φ_o, corresponds to that of an infinite medium, and therefore differs from the experimentally observed value, which is inevitably influenced by material interfaces and other geometrical features.[66,79,80] Furthermore, Φ_o strongly depends on the local charge density in the semiconductor, which, in turn, is governed by the spatial distribution of recombination processes through the charge continuity equation. Specifically, in perovskite materials, where the recombination mechanisms are known to be monomolecular -trap-assisted, bimolecular -radiative, and Auger, the continuity equation for the charge carrier density can be defined as follows:

$$\frac{dn}{dt} = G - k_1 n(\mathbf{r}) - F(\mathbf{r})k_2 n^2(\mathbf{r}) - k_3 n^3(\mathbf{r}) \quad (3)$$

where G denotes the charge generation rate, that can result from either irradiance absorption or current injection in a photoluminescence (PL) or electroluminescence (EL) framework, respectively. The constants k_1, k_2 and k_3 are rate coefficients corresponding to trap-assisted, radiative and Auger recombination processes, respectively.[16,66,81] Importantly, both the carrier density n and the Purcell factor F are spatially dependent quantities ($\mathbf{r}$), due to the local variation of the optical environment introduced by geometry and material distribution. Since a perfectly balanced charge carrier density is assumed, we use a single carrier density n to indistinguishable represent both electron and hole densities. In addition, excitonic effects are not included in this model, which would require a more complex set of equations.[82,83]

Results and discussion

The reference PeLED device (without NPs) uses a standard architecture for green photon emission, shown in Fig. 1a. It consists, from top to bottom, of glass, indium-doped tin oxide (ITO) as transparent contact, poly(3,4-ethylenedioxythiophene) (PEDOT) as HTL, CsPbBr$_3$ as the EML, 1,3,5-Tris[(pbiphenyl)-2-yl]benzene (TPBi) as ETL, and aluminium (Al) as back contact. Band to band spontaneous emission processes can be modelled as a dipole transition, where the recombining hole–electron pair acts as an oscillating electric dipole, emitting electromagnetic radiation in accordance with classical electrodynamics and quantum mechanical dipole transition theory.[76] As depicted in the figure, individual dipole sources are located along the vertical axis, z, to obtain the contribution to the emitted light coming from specific height, z_i, at the EML. For this simple 1D reference system, simulations are performed using Optical Multilayer Simulator from Lumerical Inc.,[84] based on the Transfer Matrix Method (TMM).[85] In each calculation, a single dipole source is placed at a specific vertical position z_i within the perovskite layer. To model an isotropic emission source, three orthogonal dipole orientations along the x, y and z directions are considered. The total emission response is obtained by sweeping the perovskite film thickness, performing successive calculations with the dipole source at different z_i, averaging the individual contributions from each dipole polarization. More details about these simulations, as well as the employed spectral complex refractive indices[86–90] to optically characterize all the materials in the PeLED architecture, are provided in the SI A (Fig. S1–S3). Fig. 1b shows normalized curves of both the extinction coefficient (k) and the pristine PL spectrum of the CsPbBr$_3$ perovskite.[55] As observed, the absorption of the material decays until it vanishes at its bandgap wavelength, at $\lambda_g = 530$ nm, while the PL distribution is centred at $\lambda_o = 514$ nm, providing green emission. The spectral overlap of these curves, due to the small Stokes shift,[66–69] facilitates the PR effect, which will significantly enhance the PeLED efficiency, as discussed later.

Triangle-shaped colour map in Fig. 1c represents the outcoupling efficiency of monochromatic dipole sources centred at λ_o. The total perovskite thickness is varied from $Z = 10$ nm to 300 nm, thus changing the available z_i positions for locating the dipole source, providing the triangled-shaped distribution. As observed, there is a progressive transition from one to three outcoupling maxima modes within the EML as the thickness is enlarged. Vertical dashed lines highlight the specific thicknesses $Z = 50$ nm and $Z = 150$ nm, corresponding to thin and thick EML thickness, for which the effect of incorporating plasmonic NPs will be evaluated. These values were selected because the thinner layer represents a typical PeLED architecture, exhibiting a monomodal behaviour centred at mid-height, while the thicker layer accommodates a broader range of NP sizes, enabling the tuning of plasmonic resonances over broader extents.

The 3D plasmonic PeLED is modelled with the inclusion of a single metal NP of radius R positioned at the centre of the perovskite EML. Assuming the NP is at the centre of the perovskite film is a reasonable approximation given the relative sizes of the NP and the film thickness.[91] FDTD simulations are performed using the 3D Electromagnetic Simulator from Lumerical Inc.,[84] employing perfect matching layers (PMLs) in all system directions to absorb outgoing waves. By doing so, we assume no interaction among different particles, a valid approximation for low particle concentration devices, as here considered. The glass substrate dimensions significantly exceed both the scale of the studied system and the emitted wavelength, allowing interference effects within the layer to be neglected. Therefore, it is modelled as a semi-infinite layer by placing a PML within it, assuming a non-absorbing medium with a constant refractive index ($N_{glass} = 1.5$). The electromagnetic field profile at the glass substrate is recorded, allowing the calculation of the fraction of power emitted upwards. This is then projected to the far-field using plane-wave expansion and Fresnel coefficients transformation to account for the refractive index change from glass to air (i.e., $N_{air} = 1$), providing angularly resolved information on the radiation emitted outside the device. As illustrated in Fig. 2a, due to the rotational symmetry of the system, simulations are performed by sweeping the
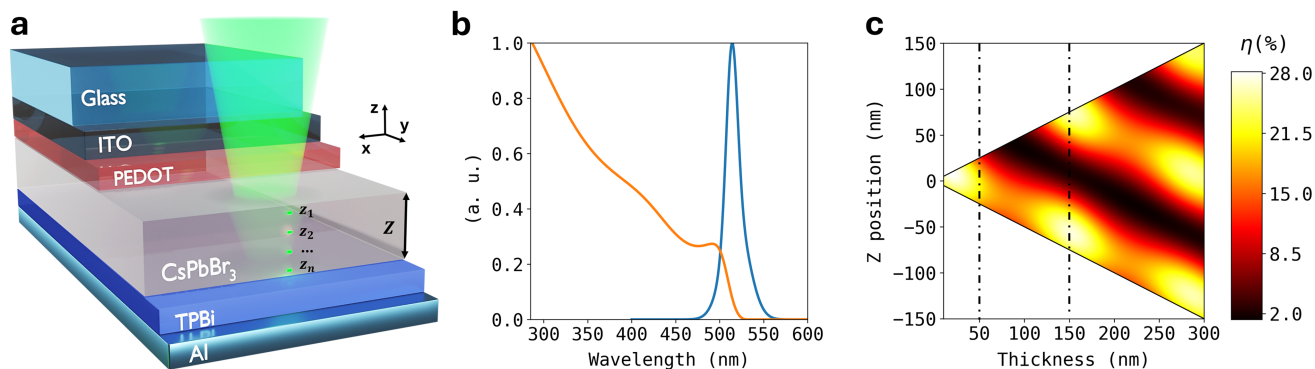
Fig. 1 (a) Illustrative scheme of the simulated PeLED device architecture: glass/ITO (150 nm)/PEDOT (14 nm)/CsPbBr$_3$ (Z)/TPBi (60 nm)/Al (100 nm). (b) Normalized extinction coefficient (orange) and PL spectrum (blue) of the CsPbBr$_3$ perovskite with bandgap λ_g = 530 nm, showing the overlapping between the absorption and the emission, which is centred at λ_o = 514 nm. (c) Colour map of the outcoupling efficiency as a function of the perovskite layer thickness, considering the spatial contribution of independent dipoles located along the Z position, z_i. The local contribution within the EML vertical axis is depicted, exhibiting multimodal outcoupling patterns that change with the thickness. Vertical dashed lines correspond to total thicknesses of Z = 50 nm and Z = 150 nm, showing one or two outcoupling maxima, respectively, which are chosen for further analysis embedding plasmonic NPs.

isotropic point-like source positions along the (x, z) plane, which bisects the spherical NP, ensuring that the plane cuts the sphere into two symmetrical halves. We refer the reader to SI A and Fig. S4 to see more information on the details of the FDTD simulations and the employed computational setup.

Both the calculated electric power emitted by each individual source, $P_{in}(x, z)$, and their corresponding outcoupled power, $P_{out}(x, z)$, are normalised to the analytical expression for the total radiated power of an electric dipole in a homogeneous medium (see SI A), where the refractive index corresponds to that of the emitting perovskite. Note that $P_{in}(x, z)$ is in fact, by definition, the Purcell factor — the emission ratio within the system compared to an infinite medium. Exploiting the rotational symmetry, the total density power $\overline{P_{out}}$ emitted by the system can be calculated integrating over a chosen cylinder volume V of radius R_c, thus $\overline{P_{out}} = \int P_{out} dV/(\pi R_c^2)$. In this regard, the choice on R_c sets the volume of the system, which in turn sets the particle volume concentration (C) of the NP in the EML, defined as $C(\%) = \dfrac{4/3\pi R^3}{\pi Z R_c^2} \times 100$. Fig. 2b shows the calculated total power density in PeLEDs of Z = 50 nm, incorporating Ag NPs of varying sizes and concentrations. To avoid plasmonic coupling between particles, the maximum particle concentration was limited to 30%.[65] Under these conditions, the enhanced far-field radiated power can be attributed solely to the presence of isolated spheres, without contributions from collective or array-induced effects. These results are then compared to the power density from a reference system (i.e., the same architecture without NPs). It can be seen that R = 15 nm Ag NPs, at concentrations between 15% and 20%, result in approximately 8-fold enhancement in the far-field dipole emission. In contrast, spherical Au NPs were also studied, and exhibited significantly lower performance, with noticeable emission quenching, as seen in Fig. S5 in SI B. Therefore, the optimal system, with 15 nm Ag NPs will be the focus of study in the following sections. However, it is important to note that this

enhancement in dipole emission does not directly translate to a similar improvement in the overall performance of the PeLED. As will be discussed later, when considering real material properties and charge carrier dynamics, this radiative enhancement is limited by the number of injected carriers and the presence of non-radiative recombination pathways, which will impact the overall efficiency. While our model provides valuable insights into the effects of plasmonic NPs on PeLEDs, it is based on certain assumptions, such as the lack of interaction between NPs and the simplification of charge carrier dynamics. These assumptions may limit the model's ability to capture all the physical effects in a real device, particularly at higher NP concentrations or in systems with more complex charge transport behaviours. Thus, future research should refine the model to include more complex interactions and dynamics to better represent all type of real-world conditions.

The directionality of the emitted light from Ag NPs-embedded devices is also analysed. The polar plot in Fig. 2c shows the far-field angular radiated power distribution for the different explored plasmonic PeLEDs of Z = 50 nm thickness. It can be observed that all the curves reveal a negligible modification in directionality, following an angle distribution very similar to Lambertian profiles, slightly modified mostly due to refraction and interference effects occurring in the device. Subsequently, $\overline{P_{out}}$ from the Z = 150 nm PeLEDs, where the increased thickness allows for a greater variation of NP radii, is shown in Fig. 2d. For the smaller tested radii of R = 20 nm, R = 35 nm and R = 50 nm, results show a noticeable improvement in power density emission compared to the reference, though this enhancement is not as pronounced as in the case of Z = 50 nm. On the other hand, larger NPs, i.e., R = 65 nm, lead to emission quenching, with the radiated power failing to surpass that of the reference system. Additionally, more interesting results are obtained for emission directionality, as displayed in Fig. 2e. Radiated angular distributions from the R = 20 nm, R = 35 nm and R = 50 nm NP systems are presented alongside those
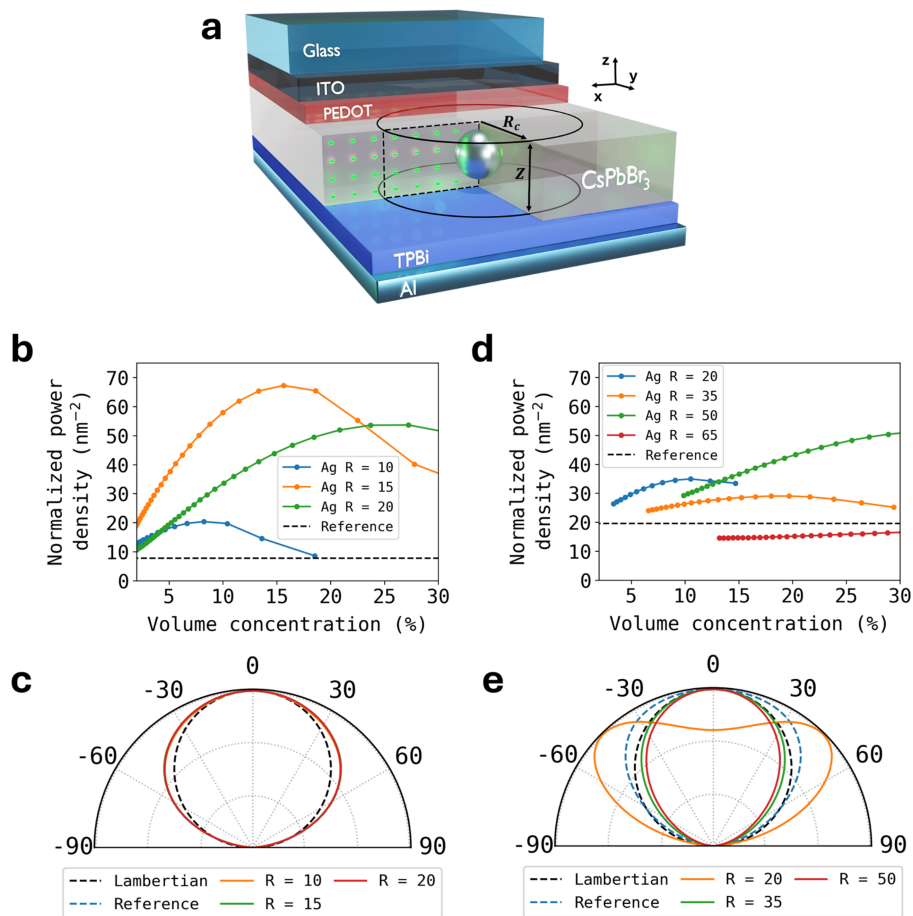
Fig. 2 (a) Scheme of the simulated plasmonic PeLED device, where the cylindric symmetry is illustrated. (b) Power radiated by dipoles to the far field in a $Z = 50$ nm system as a function of the NPs volume concentrations, for different sphere radius $R = 10$ nm (blue), $R = 15$ nm (orange) and $R = 20$ nm (green). Results are compared to those of a reference system (*i.e.*, devices without NPs) represented with a black dashed line. (c) Corresponding polar plot of the angular distribution of the power emitted to the far field compared to a Lambertian profile. The represented curves overlap in all cases (including the reference system, demonstrating the lack of modification in directionality. (d) Analogous results for a $Z = 150$ nm perovskite layer, incorporating $R = 20$ nm (blue), $R = 35$ nm (orange), $R = 50$ nm (green) and $R = 65$ nm (red). (e) Analogous polar plot for a $Z = 150$ nm PeLED. A change in directionality behaviour can be observed, establishing angular distribution broadening ($R = 20$ nm) and narrowing ($R = 35$, $R = 50$ nm), in comparison to the reference PeLED.

of the reference and a Lambertian profile, exhibiting an evident modification in their directional properties. While the former showcases a broadened profile resulting in diffuse emission, the others exhibit the opposite behaviour, narrowing the emission angles and focusing outcoupled light towards the forward direction. Although this aspect was not further explored in this work, we would like to highlight the potential applications of this finding in achieving tailored lighting properties to meet specific requirements. The optimization of plasmonic NP size and concentration not only enhances the spontaneous emission in these devices but also paves the way for tuneable directional emission when combined with appropriate EML thicknesses. Additional results showing the variation in far-field angular distribution as a function of NP concentration can be found in Fig. S6.

The analysis presented here corresponds to the record-performing NP configuration ($R = 15$ nm), for which an extensive simulation effort was carried out. A total of 1104 dipole positions were considered, excluding those falling inside the NP volume (which amount to 148), and each was simulated under three orthogonal polarizations—resulting in 2868 individual FDTD simulations. The spatial distribution of the Purcell factor corresponding to each individual dipole source is represented in Fig. 3a, showcasing extremely high values at the NP surroundings, benefiting from the near-field enhancement induced by the LSPRs. However, even an infinitely high Purcell factor cannot push the QY beyond 1 (see eqn (3)), ultimately relativizing the emission of the device to the number of available charge carriers, and the non-radiative pathways, which remain unaffected. For this reason, the enhancement in EQE will not be as pronounced as the above reported radiated power improvements in dipolar emissions, at least when the intrinsic quantum yield (Φ_o) of the material is sufficiently high. The corresponding spatial outcoupling efficiency is depicted in Fig. 3b, where it can be observed that extraction of light is lower near the NP. This light trapping is associated with stronger
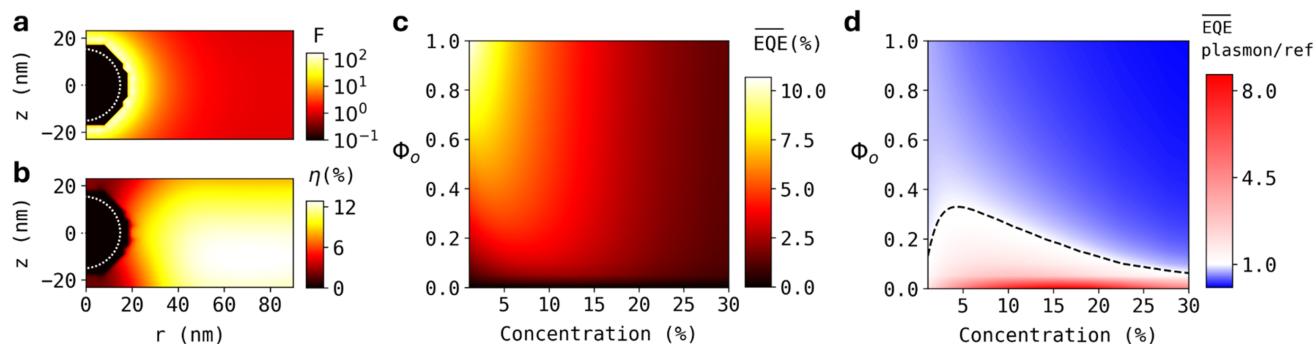
Fig. 3 (a) Colormap of the calculated Purcell factor (log scale) over the perovskite layer in the optimal plasmonic PeLED ($Z = 50$ nm, $R = 15$ nm). As a guide to the eye, dashed white line describe the particle shape. To avoid numerical divergences, dipoles are not placed within a buffer zone extending 4 nm (2 mesh cells) from the nanoparticle surface. This exclusion region appears as a dark shell surrounding the particle. (b) Corresponding colormap of the outcoupling efficiency. (c) $\overline{EQE}$ results for the plasmonic PeLED device calculated as a function of the NP concentration (x-axis) and the intrinsic quantum yield, Φ_o (y-axis), of the material. (d) Comparison between the $\overline{EQE}$ of the plasmonic and the reference systems are depicted. The dashed black line marks the unity contour, separating the region where $\overline{EQE}$ is enhanced by plasmonic effects (lower red area) from the region where efficiency is reduced (upper blue area).

scattering effects due to strong LSPRs, revealing a double-edged nature of plasmonic effects in our system. While near-field plasmonic effect contribute to enhanced QY, scattering may lead photons into waveguide modes, preventing them to be extracted outside the device. By convoluting both the QY and the outcoupling efficiency, the effective $\overline{EQE}$ of the system can be calculated as follows:

$$\overline{EQE}(R_c, \Phi_o) = \frac{2}{ZR_c^2} \int_0^{R_c} \int_{-Z/2}^{Z/2} \Phi(\Phi_o, r, z)\eta(r, z)r\,dz\,dr \quad (4)$$

with z and r being the vertical and radial components in cylindric coordinates. Fig. 3c shows the calculated $\overline{EQE}$s results when no PR phenomena are considered. The plot displays a sweep of intrinsic quantum yield values, Φ_o (y-axis), alongside a sweep in cylinder radii, which determine the NP concentration (x-axis). As expected, the $\overline{EQE}$ values increase with the emissive quality of the material, quantified by the intrinsic Φ_o, reaching $\overline{EQE}$s values higher than 10%. The comparison between the plasmonic and the reference system is displayed in Fig. 3d, where the corresponding $\overline{EQE}$s values are expressed as the ratio between the plasmonic and the reference cases. The depicted dashed black line represents the unity contour line, delimiting the region of plasmonically enhanced $\overline{EQE}$ (lower part of the panel, in red colour) with respect to the region in which the efficiency is reduced (higher part of the panel, in blue). This reveals that, since two competing effects are at play, only the systems with initial low emissive materials, *i.e.*, low intrinsic quantum yield values, $\Phi_o < 0.3$, benefit from enough radiative enhancement to be able to overcome the losses in extraction efficiency.

At first glance, the results just presented suggest that the inclusion of plasmonic NPs may not be as beneficial as initially expected. However, the analysis so far has not considered the PR effect, which is crucial to realistically model light–matter interactions within perovskites, especially when the number of trapped photons due to scattering effects increases. To address

this, a PR model has been developed to accurately calculate a realistic outcoupling efficiency. As schematised in Fig. 4a, photons undergoing reflections back into the EML interfaces due to their high-angle trajectories will couple to trapped modes. As a consequence of the small Stokes shift present in perovskite materials, a reabsorption and subsequent reemission at any wavelength in the PL of those trapped photons becomes possible, opening a new chance for these to be outcoupled from the PeLED. Understanding this as an iterative process, in which the fraction of recycled photons, ρ, can be reused in subsequent PR events, the corrected outcoupling efficiency can be expressed as a power series, as in eqn (5a), where η_0 denotes the initially calculated outcoupling efficiency. Note that the second equality arises from considering an infinite number of PR events ($m \rightarrow \infty$), valid for $|\rho| < 1$. The recycling probability is calculated as expressed in eqn (5b), where S and A represent, respectively, the probability of being trapped and reabsorbed. We refer the reader to SI C where more information on the model is given.

$$\eta_m = \eta_0 + \eta_0\rho + \eta_0\rho^2 + \ldots + \eta_0\rho^m = \frac{1}{1-\rho}\eta_0 \quad (5a)$$

$$\rho = S \cdot A \cdot \Phi \quad (5b)$$

The QY of the device is dependent on the availability of charge carriers to recombine, so the current injected in the device must be considered to properly characterize the EQE. Assuming an ideal carrier diffusivity behaviour without any electrical losses, we substitute the generation rate in eqn (3) by the number of injected charges $\frac{J}{Z \cdot e}$, where J represents the injection current density and e denotes the elementary charge. Solving eqn (3) at each spatial point in the system gives the charge density distribution, from which an effective QY can be calculated for further analysis:
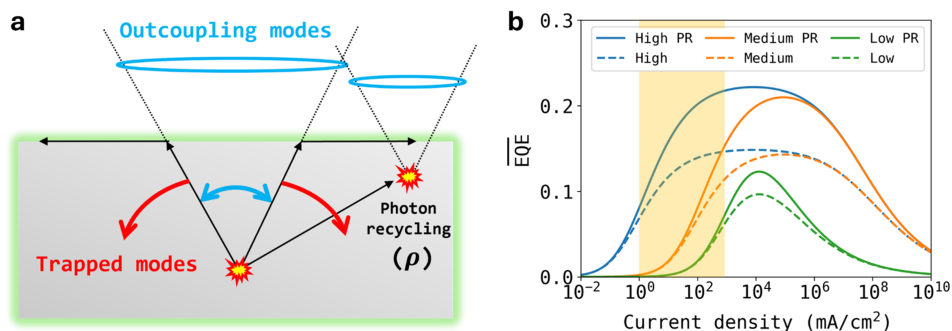
Fig. 4 (a) Illustration of the photon recycling process. Trapped photons can be re-absorbed for further re-emission, increasing the effective outcoupling of the device. (b) $\overline{EQE}$ for a PeLED device without plasmonic NPs either including photon recycling PR effects (solid lines) or not (dashed lines). Calculations are performed as a function of the injected current density for three different performing perovskites: high-performing ($k_1 = 10^6$ s^{-1}, $k_2 = 10^{-9}$ cm^3 s^{-1}, $k_3 = 10^{-28}$ cm^6 s^{-1}), medium performing ($k_1 = 10^7$ s^{-1}, $k_2 = 10^{-9}$ cm^3 s^{-1}, $k_3 = 10^{-28}$ cm^6 s^{-1}), and low performing ($k_1 = 10^7$ s^{-1}, $k_2 = 10^{-10}$ cm^3 s^{-1}, $k_3 = 10^{-28}$ cm^6 s^{-1}), revealing the different regions governed by different recombination mechanisms. The yellow band represents the usual current density operation range for which EQEs are maximized in state-of-the-art PeLEDs.[24–26]

$$\Phi(\mathbf{r}) = \frac{F(\mathbf{r})k_2 n(\mathbf{r})}{k_1 + F(\mathbf{r})k_2 n(\mathbf{r}) + k_3 n^2(\mathbf{r})} \quad (6)$$

Fig. 4b shows the calculated $\overline{EQE}$ of the reference system as a function of the current density for different hypothetical device performances. The displayed curves are calculated considering different k_1, k_2 and k_3 combinations ranging within reported values,[15,16,81,83,92,93] with representative values describing low-, medium- and high-performing perovskite materials. A yellow band representing the usual current density operation range for which EQEs are maximized in state-of-the-art PeLEDs[24–26] is also shown. The results highlight the impact of PR effects, revealing a significant enhancement in EQE driven by improved outcoupling efficiency. This enhancement exceeds the classical ray-optics limit of $1/2\mathrm{Re}(N_{EML})^2$,[94,95] which assumes no interference effects typically present in thin-film structures. Here, N_{EML} refers to the complex refractive index of the emitting material, which in our perovskite is approximately 2, setting a theoretical limit near 12.5%. This aligns well with our calculated $\overline{EQE}$ values (dashed lines), which range from 10 to 15% under realistic device conditions. Notably, when PR is included, simulated $\overline{EQE}$ exceed 22% for high-performing perovskites, consistent with reported values.[71] In all curves, different regimes can be observed depending on the injected current. At low injection currents, trap-assisted recombination, that scales linearly with the population density, is the dominant mechanism. The constant k_1 that governs its behaviour accounts for the presence of trap states induced by defects and impurities, and its values roughly ranges between 10^6–10^7 s^{-1}. In this regime, radiative recombination is effectively suppressed, leading to negligible $\overline{EQE}$ values. Then, for higher currents at which the bimolecular recombination mechanism governed by k_2 (roughly 10^{-9}–10^{-10} cm^3 s^{-1}) starts dominating, spontaneous emission that scales with n^2 becomes stronger and the EQE starts taking off. At considerable higher currents, Auger recombination processes involving inelastic scattering between more than two particles appears, quenching the emissivity of the material. It is worth noting that, for reported values of $k_3 \sim$ 10^{-28} cm^6 s^{-1}, the onset of the Auger-dominated regime occurs at high current densities, well beyond the typical low-power operating conditions of PeLEDs. Nevertheless, highly bright devices for applications such as outdoor displaying, large-scale signage or long-range optical communications, could experience current-efficiency roll-off when Auger recombination becomes a limiting factor.[15,16]

In the following, the EQE results for plasmonic systems using the record NP ($R = 15$ nm), and including PR effects, are discussed. We also want to highlight that, in plasmonic systems, due to increased trapped states caused by scattering effect, PR effects become more evident, helping to mitigate the decrease in outcoupling that was significantly reducing the EQE. The comparison between calculations including and excluding the PR effect can be found in Fig. S7. Fig. 5(a–c) shows the $\overline{EQE}$ contour plots for the same three performing (high, medium, low) perovskite-based devices as those considered in Fig. 4b, but including plasmonic effects. Their comparison with respect to the reference system under the same working conditions are shown in Fig. 5(d–f). For high-performing perovskite devices, the incorporation of plasmonic NPs leads to $\overline{EQE}$ enhancement only at low injected currents (<1 mA cm^{-2}), where the reduced QY of the reference PeLED leads to negligible radiative output. This implies that the radiative threshold of the device can be significantly lowered by plasmonic enhancement. As a result, the system becomes capable of emitting efficiently at ultra-low injection levels—regimes where the reference (non-plasmonic) device remains effectively non-emissive. In other words, plasmonic effects unlock low-power operation that would otherwise be unattainable. In fact, as shown in detail in Fig. S8, $\overline{EQE}$s values of 6% and 2% are achieved at current densities as low as 0.2 mA cm^{-2}, and 0.02 mA cm^{-2}, respectively. Translating these values into power densities, and based on state-of-the-art PeLED studies that report J–V curves,[24–26] our designs demonstrate ultra-low power operation at 0.4 mW cm^{-2} and 0.02 mW cm^{-2}, respectively. Indeed, when compared to commercial devices labelled as very low-power consumption LEDs (e.g., 4 mW), these values represent
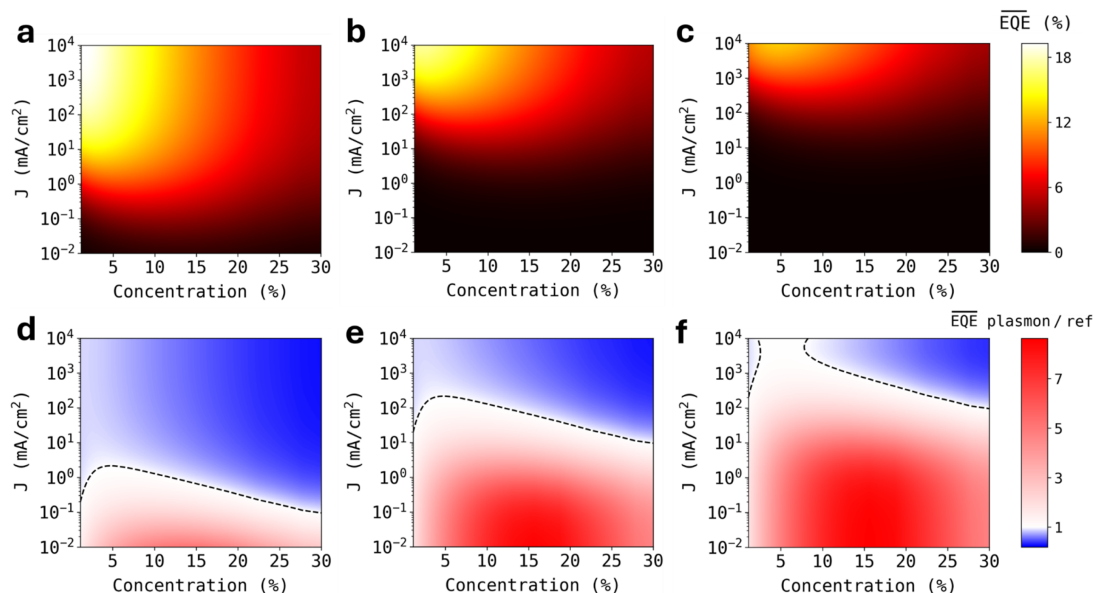
Fig. 5 (a–c) Calculated $\overline{EQE}$s values for the plasmonic system as a function of the current density and NP concentration. Simulations are performed for three types of perovskite materials: high-performing ($k_1 = 10^6$ s^1, $k_2 = 10^{-9}$ cm^3 s^1, $k_3 = 10^{-28}$ cm^6 s^1), medium-performing ($k_1 = 10^7$ s^1, $k_2 = 10^{-9}$ cm^3 s^1, $k_3 = 10^{-28}$ cm^6 s^1) and low-performing ($k_1 = 10^7$ s^1, $k_2 = 10^{-10}$ cm^3 s^1, $k_3 = 10^{-28}$ cm^6 s^1). (d–f) Corresponding $\overline{EQE}$s enhancement maps compared to the reference (non-plasmonic) system. The dashed black line marks the unity contour, separating the region where $\overline{EQE}$ is enhanced by plasmonic effects (lower red area) from the region where efficiency is reduced (upper blue area). At low current densities, these results highlight the potential for energy-efficient applications. The enhancement becomes more pronounced as nonradiative losses increase, illustrating the ability of plasmonic structures to induce defect tolerance and expand the operational versatility of PeLEDs.

a reduction of approximately 3 and 4 orders of magnitude in power consumption for a hypothetical device with equivalent surface area (e.g., 1 mm^2).[96–99] These results highlight the potential of plasmonic PeLEDs as highly efficient, ultra low-power light sources for applications such as IoT devices, wearables, and other energy-constraint technologies.

Additionally, it is observed that as the performance of the perovskite material decreases, the threshold current below which the plasmonic system exhibits $\overline{EQE}$ enhancement (depicted with the dashed black line) increases. This indicates that the beneficial effects of embedding plasmonic NPs are more pronounced in lower-performing devices. Even for high-performing devices, the incorporation of plasmonic NPs yields EQE enhancement under low injection currents. Interestingly, for medium-performing perovskite-based devices, modelled by increasing k_1 to 10^7 s^{-1}, indicating a higher density of trap states, the enhancement threshold shifts to significantly higher current densities, in the range of 10–100 mA cm^{-2}. This range notably overlaps with the typical operating regime of PeLEDs, suggesting that plasmonic integration may provide tangible performance benefits under realistic device conditions. These results reveal that the use of plasmonic NPs integrated into the EML can provide devices with greater tolerance to defects in the emitting material. Furthermore, as seen in the low-performing case, the effect is more evident for low emitting material where the k_2 was decreased to 10^{-10} cm^3 s^{-1}. Here, the radiative threshold of the plasmonic system is further lowered with respect to the reference, even promising a radiative regime at standard operation currents for which the reference device

would barely emit light. In addition, other calculations have been performed in which k_3 was increased, as shown in Fig. S9. In them, plasmonic systems also exhibit improvements at high currents, indicating a delay in the onset of the Auger-dominated regime. Altogether, the results demonstrate that integrating plasmonic NPs into the EML can enhance device versatility and robustness across a wider range of injection levels. This enables PeLED operation at lower currents, thereby reducing adverse thermal effects associated with high charge population, and high currents, thus enabling highly bright devices. By strategically incorporating plasmonic NPs into PeLEDs, we are not only enhancing emission efficiency but also enabling low-power operation suitable for energy-sensitive applications. This approach holds promise for devices such as portable electronics, efficient lighting, and low-power displays, where minimizing energy consumption without sacrificing brightness or performance is paramount. As we continue refining this technology, we envision plasmonic PeLEDs playing a key role in shaping the future of compact, energy-efficient lighting solutions for a wide range of practical applications. However, it is worth noting that significant enhancements are only achieved when the size, concentration, and placement of the NPs are carefully optimized based on a rigorous theoretical design. Indiscriminate NP integration often fails to deliver noticeable benefits and can even be detrimental to device performance. Finally, the long-term stability of PeLEDs incorporating plasmonic NPs must be considered. While the improvements in emission and EQE are promising, further studies should assess the impact of NP integration on the material degradation and

long-term operational stability of the devices,[18,32,100] including possible contributions from local photothermal heating or electric-field-driven ion migration. Although such effects are expected to remain minimal under the ultra-low current densities primarily considered in this work, they represent important aspects to be addressed in future experimental validation.

Conclusions

In this work, we have developed an advanced FDTD-based volumetric model to investigate the complex emission characteristics of PeLEDs, integrating photon recycling and plasmonic effects. Our results show that incorporating 15 nm Ag NPs into a device with a 50 nm thick $CsPbBr_3$ perovskite layer leads to an 8-fold enhancement in dipole emission into the far-field. However, this comes with a trade-off: the Purcell enhancement improves spontaneous emission, while the strong plasmonic scattering can hinder light extraction, reducing outcoupling efficiency.

Moreover, our analysis demonstrates that the size of the NPs can influence the emission directionality, with a shift from diffuse emission to more directional, forward-directed emission, as the NP size and perovskite thickness varies. This ability to control the angular distribution of emitted light presents opportunities for tailoring emission profiles, which could be useful for applications requiring precise light directionality.

Further, our EQE analysis highlights the potential of plasmonic PeLEDs for low-power operation. The integration of plasmonic NPs shifts the radiative recombination threshold to lower injection currents, thereby improving the device's tolerance to trap-assisted recombination, especially in scenarios where material defects or fabrication imperfections are a limiting factor. On the other hand, the reduction of Auger recombination due to plasmonic effects results in reduced current-efficiency roll-off, further enhancing the device's ability to operate at high currents.

Despite these promising results, it is essential to note that incorporating plasmonic NPs into the PeLED system requires careful design. Simply adding NPs without consideration of their size, concentration, and placement could lead to suboptimal performance. Thus, a well-optimized design is necessary to maximize the benefits of plasmonic enhancements. Importantly, these findings also provide chemical and structural design guidelines for tailoring perovskite-plasmonic hybrid systems, offering insights relevant to the composition, morphology, and integration strategies of next-generation optoelectronic materials. Moreover, while our results indicate significant improvements in emission and efficiency, the long-term stability and scalability of this approach need to be further investigated to ensure its applicability in real-world scenarios. Future research should focus on refining fabrication processes and evaluating the impact of plasmonic NPs on the durability and performance of PeLEDs under operational conditions, including potential effects such as local photothermal heating or field-induced ion migration that could compromise stability.

Conflicts of interest

There are no conflicts to declare.

Data availability

All data included in this study are available from the corresponding authors upon request.

Supplementary information: complex refractive indices, TMM and FDTD simulation details, emission from plasmonic PeLEDs employing Au NPs, angular distribution of emission, photon recycling model details, and extended results regarding EQE optimization at low and high injection currents. See DOI: https://doi.org/10.1039/d5ra05461c.

References

1 C. Bao, *et al.*, High Performance and Stable All-Inorganic Metal Halide Perovskite-Based Photodetectors for Optical Communication Applications, *Adv. Mater.*, 2018, **30**, 1803422.

2 Q. Shan, *et al.*, Perovskite light-emitting/detecting bifunctional fibres for wearable LiFi communication, *Light: Sci. Appl.*, 2020, **9**, 163.

3 D. Karunatilaka, F. Zafar, V. Kalavally and R. Parthiban, LED Based Indoor Visible Light Communications: State of the Art, *IEEE Commun. Surv. Tutor.*, 2015, **17**, 1649–1678.

4 Y. Zhao, X. Guo, H. Sun and L. Tao, Recent Advances in Flexible Wearable Technology: From Textile Fibers to Devices, *Chem. Rec.*, 2024, **24**, e202300361.

5 E. H. Cho, *et al.*, Wearable and Wavelength-Tunable Near-Infrared Organic Light-Emitting Diodes for Biomedical Applications, *ACS Appl. Mater. Interfaces*, 2023, **15**, 57415–57426.

6 L. Veeramuthu, *et al.*, Human Skin-Inspired Electrospun Patterned Robust Strain-Insensitive Pressure Sensors and Wearable Flexible Light-Emitting Diodes, *ACS Appl. Mater. Interfaces*, 2022, **14**, 30160–30173.

7 Z. Liu, W. C. Chong, K. M. Wong and K. M. Lau, GaN-based LED micro-displays for wearable applications, *Microelectron. Eng.*, 2015, **148**, 98–103.

8 J. Kim, *et al.*, Ultrathin Quantum Dot Display Integrated with Wearable Electronics, *Adv. Mater.*, 2017, **29**, 1700217.

9 S. Chang, *et al.*, Flexible and Stretchable Light-Emitting Diodes and Photodetectors for Human-Centric Optoelectronics, *Chem. Rev.*, 2024, **124**, 768–859.

10 F. Falchi, *et al.*, The new world atlas of artificial night sky brightness, *Sci. Adv.*, 2016, **2**, e1600377.

11 C. Liu, B. Li and M. Qiu, Advancements in the Improvement of Optical Outcoupling Efficiency for Perovskite LEDs, *Adv. Devices Instrum.*, 2024, **5**, 0045.

12 G. Lampropoulos, K. Siakas and T. Anastasiadis, Internet of things in the context of industry 4.0: an overview, *Int. J. Entrep. Knowl.*, 2019, **7**, 4–19.

13 C. Weisbuch, *et al.*, The efficiency challenge of nitride light-emitting diodes for lighting, *Phys. Status Solidi A*, 2015, **212**, 899–913.

14 N. Li, *et al.*, Ultra-low-power sub-photon-voltage high-efficiency light-emitting diodes, *Nat. Photonics*, 2019, **13**, 588–592.

15 Z. Li, *et al.*, Highly bright perovskite light-emitting diodes enabled by retarded Auger recombination, *Nat. Commun.*, 2025, **16**, 927.

16 C. Zou, Y. Liu, D. S. Ginger and L. Y. Lin, Suppressing Efficiency Roll-Off at High Current Densities for Ultra-Bright Green Perovskite Light-Emitting Diodes, *ACS Nano*, 2020, **14**, 6076–6086.

17 L. Zhao, *et al.*, Thermal Properties of Polymer Hole-Transport Layers Influence the Efficiency Roll-off and Stability of Perovskite Light-Emitting Diodes, *Nano Lett.*, 2023, **23**, 4785–4792.

18 L. Zhao, *et al.*, Thermal Management Enables Bright and Stable Perovskite Light-Emitting Diodes, *Adv. Mater.*, 2020, **32**, 2000752.

19 X. Li, *et al.*, Bright colloidal quantum dot light-emitting diodes enabled by efficient chlorination, *Nat. Photonics*, 2018, **12**, 159–164.

20 S. A. Veldhuis, *et al.*, Perovskite Materials for Light-Emitting Diodes and Lasers, *Adv. Mater.*, 2016, **28**, 6804–6834.

21 L. Zhu, *et al.*, Unveiling the additive-assisted oriented growth of perovskite crystallite for high performance light-emitting diodes, *Nat. Commun.*, 2021, **12**, 5081.

22 X.-K. Liu, *et al.*, Metal halide perovskites for light-emitting diodes, *Nat. Mater.*, 2021, **20**, 10–21.

23 S. D. Stranks and H. J. Snaith, Metal-halide perovskites for photovoltaic and light-emitting devices, *Nat. Nanotechnol.*, 2015, **10**, 391–402.

24 W. Bai, *et al.*, Perovskite Light-Emitting Diodes with an External Quantum Efficiency Exceeding 30%, *Adv. Mater.*, 2023, **35**, 2302283.

25 M. Li, *et al.*, Acceleration of radiative recombination for efficient perovskite LEDs, *Nature*, 2024, **630**, 631–635.

26 J. Jiang, *et al.*, Red Perovskite Light-Emitting Diodes with Efficiency Exceeding 25% Realized by Co-Spacer Cations, *Adv. Mater.*, 2022, **34**, 2204460.

27 W. Zhou, *et al.*, Manipulating Ionic Behavior with Bifunctional Additives for Efficient Sky-Blue Perovskite Light-Emitting Diodes, *Adv. Funct. Mater.*, 2023, **33**, 2301425.

28 J. Chen, *et al.*, Efficient and bright white light-emitting diodes based on single-layer heterophase halide perovskites, *Nat. Photonics*, 2021, **15**, 238–244.

29 J. S. Kim, *et al.*, Ultra-bright, efficient and stable perovskite light-emitting diodes, *Nature*, 2022, **611**, 688–694.

30 H. Liu, *et al.*, Large-Area Flexible Perovskite Light-Emitting Diodes Enabled by Inkjet Printing, *Adv. Mater.*, 2024, **36**, 2309921.

31 X. Yang, *et al.*, Towards micro-PeLED displays, *Nat. Rev. Mater.*, 2023, **8**, 341–353.

32 B. Zhao, *et al.*, Highly stable perovskite light-emitting diodes, *Matter*, 2024, **7**, 772–793.

33 Y. Hassan, *et al.*, Ligand-engineered bandgap stability in mixed-halide perovskite LEDs, *Nature*, 2021, **591**, 72–77.

34 B. Zhao, *et al.*, Light management for perovskite light-emitting diodes, *Nat. Nanotechnol.*, 2023, **18**, 981–992.

35 Q. Zhang, *et al.*, Light Out-Coupling Management in Perovskite LEDs—What Can We Learn from the Past?, *Adv. Funct. Mater.*, 2020, **30**, 2002570.

36 L. Lin, R. Proietti Zaccaria, D. Garoli and R. Krahne, Photonic Cavity Effects for Enhanced Efficiency in Layered Perovskite-Based Light-Emitting Diodes, *Nanomaterials*, 2021, **11**, 2947.

37 L. Zhao, K. M. Lee, K. Roh, S. U. Z. Khan and B. P. Rand, Improved Outcoupling Efficiency and Stability of Perovskite Light-Emitting Diodes using Thin Emitting Layers, *Adv. Mater.*, 2019, **31**, 1805836.

38 X. Shi, *et al.*, Optical Energy Losses in Organic–Inorganic Hybrid Perovskite Light-Emitting Diodes, *Adv. Opt. Mater.*, 2018, **6**, 1800667.

39 M. J. Jurow, *et al.*, Manipulating the Transition Dipole Moment of CsPbBr3 Perovskite Nanocrystals for Superior Optical Properties, *Nano Lett.*, 2019, **19**, 2489–2496.

40 S. Kumar, *et al.*, Anisotropic nanocrystal superlattices overcoming intrinsic light outcoupling efficiency limit in perovskite quantum dot light-emitting diodes, *Nat. Commun.*, 2022, **13**, 2106.

41 L. Lin, R. Krahne and R. Proietti Zaccaria, Improved Efficiency of Light-Emitting Diodes by Plasmonic Nanopatterning of the Charge-Transfer Layer, *Adv. Opt. Mater.*, 2022, **10**, 2200156.

42 J. Mao, *et al.*, Novel Direct Nanopatterning Approach to Fabricate Periodically Nanostructured Perovskite for Optoelectronic Applications, *Adv. Funct. Mater.*, 2017, **27**, 1606525.

43 D. Zhang, *et al.*, Increasing Photoluminescence Quantum Yield by Nanophotonic Design of Quantum-Confined Halide Perovskite Nanowire Arrays, *Nano Lett.*, 2019, **19**, 2850–2857.

44 Q. Zhang, *et al.*, Three-Dimensional Perovskite Nanophotonic Wire Array-Based Light-Emitting Diodes with Significantly Improved Efficiency and Stability, *ACS Nano*, 2020, **14**, 1577–1585.

45 Q. Zhang, *et al.*, Efficient metal halide perovskite light-emitting diodes with significantly improved light extraction on nanophotonic substrates, *Nat. Commun.*, 2019, **10**, 727.

46 Y. Cao, *et al.*, Perovskite light-emitting diodes based on spontaneously formed submicrometre-scale structures, *Nature*, 2018, **562**, 249–253.

47 S.-S. Meng, Y.-Q. Li and J.-X. Tang, Theoretical perspective to light outcoupling and management in perovskite light-emitting diodes, *Org. Electron.*, 2018, **61**, 351–358.

48 Y. Shen, *et al.*, High-Efficiency Perovskite Light-Emitting Diodes with Synergetic Outcoupling Enhancement, *Adv. Mater.*, 2019, **31**, 1901517.

49 S. Weng, *et al.*, Light extraction efficiency enhancement of CH3NH3PbBr3 light-emitting diodes using nanopatterned PEDOT:PSS layers, *Appl. Phys. Lett.*, 2021, **119**, 233302.

50 W. Chen, *et al.*, Overcoming the Outcoupling Limit of Perovskite Light-Emitting Diodes with Artificially Formed Nanostructures, *Adv. Mater.*, 2022, **34**, 2207180.

51 S. Rahimi, M. Eskandari and D. Fathi, New nanostructure perovskite-based light-emitting diode with superior light extraction efficiency enhancement, *Sci. Rep.*, 2024, **14**, 5500.

52 J. Cui, *et al.*, Efficient light-emitting diodes based on oriented perovskite nanoplatelets, *Sci. Adv.*, 2021, **7**, eabg8458.

53 A. Bayles, *et al.*, Localized surface plasmon effects on the photophysics of perovskite thin films embedding metal nanoparticles, *J. Mater. Chem. C*, 2020, **8**, 916–921.

54 B. Ai, Z. Fan and Z. J. Wong, Plasmonic–perovskite solar cells, light emitters, and sensors, *Microsyst. Nanoeng.*, 2022, **8**, 5.

55 Z. Y. Ooi, *et al.*, Strong angular and spectral narrowing of electroluminescence in an integrated Tamm-plasmon-driven halide perovskite LED, *Nat. Commun.*, 2024, **15**, 5802.

56 Z. Shi, *et al.*, Localized Surface Plasmon Enhanced All-Inorganic Perovskite Quantum Dot Light-Emitting Diodes Based on Coaxial Core/Shell Heterojunction Architecture, *Adv. Funct. Mater.*, 2018, **28**, 1707031.

57 X. Zhang, *et al.*, Plasmonic Perovskite Light-Emitting Diodes Based on the Ag–CsPbBr3 System, *ACS Appl. Mater. Interfaces*, 2017, **9**, 4926–4931.

58 P. Chen, *et al.*, Nearly 100% Efficiency Enhancement of CH3NH3PbBr3 Perovskite Light-Emitting Diodes by Utilizing Plasmonic Au Nanoparticles, *J. Phys. Chem. Lett.*, 2017, **8**, 3961–3969.

59 J. Liu, *et al.*, Rational Energy Band Alignment and Au Nanoparticles in Surface Plasmon Enhanced Si-Based Perovskite Quantum Dot Light-Emitting Diodes, *Adv. Opt. Mater.*, 2018, **6**, 1800693.

60 Y. Meng, *et al.*, Electrode quenching control for highly efficient CsPbBr3 perovskite light-emitting diodes *via* surface plasmon resonance and enhanced hole injection by Au nanoparticles, *Nanotechnology*, 2018, **29**, 175203.

61 Y. Zhang, *et al.*, Enhancing luminescence in all-inorganic perovskite surface plasmon light-emitting diode by incorporating Au-Ag alloy nanoparticle, *Opt. Mater.*, 2019, **89**, 563–567.

62 C. M. Lee, *et al.*, Improved device efficiency and lifetime of perovskite light-emitting diodes by size-controlled polyvinylpyrrolidone-capped gold nanoparticles with dipole formation, *Sci. Rep.*, 2022, **12**, 2300.

63 J. Bueno, S. Carretero Palacios and M. Anaya, Synergetic Near- and Far-Field Plasmonic Effects for Optimal All-Perovskite Tandem Solar Cells with Maximized Infrared Absorption, *J. Phys. Chem. Lett.*, 2024, **15**, 2632–2638.

64 S. Carretero-Palacios, A. Jiménez-Solano and H. Míguez, Plasmonic Nanoparticles as Light-Harvesting Enhancers in Perovskite Solar Cells: A User's Guide, *ACS Energy Lett.*, 2016, **1**, 323–331.

65 S. Carretero-Palacios, M. E. Calvo and H. Míguez, Absorption Enhancement in Organic–Inorganic Halide Perovskite Films with Embedded Plasmonic Gold Nanoparticles, *J. Phys. Chem. C*, 2015, **119**, 18635–18640.

66 J. M. Richter, *et al.*, Enhancing photoluminescence yields in lead halide perovskites by photon recycling and light out-coupling, *Nat. Commun.*, 2016, **7**, 13941.

67 W. Raja, *et al.*, Photon recycling in perovskite solar cells and its impact on device design, *Nanophotonics*, 2020, **10**, 2023–2042.

68 A. Bercegol, *et al.*, Quantitative optical assessment of photonic and electronic properties in halide perovskite, *Nat. Commun.*, 2019, **10**, 1586.

69 C. Cho, Y. Sun, J. You, L.-S. Cui and N. C. Greenham, Enhanced Photon Recycling Enables Efficient Perovskite Light-Emitting Diodes, *Adv. Funct. Mater.*, 2024, **34**, 2411556.

70 J. Liang, *et al.*, Ultrahigh Color Rendering in RGB Perovskite Micro-Light-Emitting Diode Arrays with Resonance-Enhanced Photon Recycling for Next Generation Displays, *Adv. Opt. Mater.*, 2022, **10**, 2101642.

71 C. Cho, *et al.*, The role of photon recycling in perovskite light-emitting diodes, *Nat. Commun.*, 2020, **11**, 611.

72 C. Cho and N. C. Greenham, Computational Study of Dipole Radiation in Re-Absorbing Perovskite Semiconductors for Optoelectronics, *Advanced Science*, 2021, **8**, 2003559.

73 S. D. Stranks, R. L. Z. Hoye, D. Di, R. H. Friend and F. Deschler, The Physics of Light Emission in Halide Perovskite Devices, *Adv. Mater.*, 2019, **31**, 1803336.

74 M. O. Scully and M. S. Zubairy, *Quantum Optics*, Cambridge University Press, Cambridge, 1997, DOI: **10.1017/CBO9780511813993**.

75 A. Jiménez-Solano, J. F. Galisteo-López and H. Míguez, Absorption and Emission of Light in Optoelectronic Nanomaterials: The Role of the Local Optical Environment, *J. Phys. Chem. Lett.*, 2018, **9**, 2077–2084.

76 E. Rosencher and B. Vinter, *Optoelectronics*, Cambridge University Press, Cambridge, 2002, DOI: **10.1017/CBO9780511754647**.

77 E. M. Purcell, H. C. Torrey and R. V. Pound, Resonance Absorption by Nuclear Magnetic Moments in a Solid, *Phys. Rev.*, 1946, **69**, 37–38.

78 K. H. Drexhage, Influence of a dielectric interface on fluorescence decay time, *J. Lumin.*, 1970, **1–2**, 693–701.

79 M. Furno, R. Meerheim, S. Hofmann, B. Lüssem and K. Leo, Efficiency and rate of spontaneous emission in organic electroluminescent devices, *Phys. Rev. B: Condens. Matter Mater. Phys.*, 2012, **85**, 115205.

80 S. D. Stranks, Nonradiative Losses in Metal Halide Perovskites, *ACS Energy Lett.*, 2017, **2**, 1515–1525.

81 Z. Chen, *et al.*, Recombination Dynamics Study on Nanostructured Perovskite Light-Emitting Devices, *Adv. Mater.*, 2018, **30**, 1801370.

82 S. D. Stranks, *et al.*, Recombination Kinetics in Organic-Inorganic Perovskites: Excitons, Free Charge, and Subgap States, *Phys. Rev. Appl.*, 2014, **2**, 034007.

83 J. A. Peters, *et al.*, Carrier recombination mechanism in CsPbBr_{3} revealed by time-resolved photoluminescence spectroscopy, *Phys. Rev. B*, 2019, **100**, 235305.

84 *Lumerical Inc*. **https://www.lumerical.com/**.

85 P. Yeh, *Optical Waves in Layered Media*, New York, NY, 1988.

86 C.-W. Chen, *et al.*, Optical properties of organometal halide perovskite thin films and general device structure design rules for perovskite single and tandem solar cells, *J. Mater. Chem. A*, 2015, **3**, 9152–9159.

87 P. B. Johnson and R. W. Christy, Optical Constants of the Noble Metals, *Phys. Rev. B*, 1972, **6**, 4370–4379.

88 T. A. F. König, *et al.*, Electrically Tunable Plasmonic Behavior of Nanocube–Polymer Nanomaterials Induced by a Redox-Active Electrochromic Polymer, *ACS Nano*, 2014, **8**, 6182–6192.

89 A. D. Rakić, Algorithm for the determination of intrinsic optical constants of metal films: application to aluminum, *Appl. Opt.*, 1995, **34**, 4755–4767.

90 M. Shin, *et al.*, Understanding the Origin of Ultrasharp Sub-bandgap Luminescence from Zero-Dimensional Inorganic Perovskite Cs4PbBr6, *ACS Appl. Energy Mater.*, 2020, **3**, 192–199.

91 S. Carretero-Palacios and H. Míguez, Absorption enhancement in perovskite cells using embedded gold nanoparticles, in *2015 European Conference on Lasers and Electro-Optics - European Quantum Electronics Conference*, Optica Publishing Group, 2015.

92 W. Rehman, *et al.*, Charge-Carrier Dynamics and Mobilities in Formamidinium Lead Mixed-Halide Perovskites, *Adv. Mater.*, 2015, **27**, 7938–7944.

93 C. Wehrenfennig, G. E. Eperon, M. B. Johnston, H. J. Snaith and L. M. Herz, High Charge Carrier Mobilities and Lifetimes in Organolead Trihalide Perovskites, *Adv. Mater.*, 2014, **26**, 1584–1589.

94 N. C. Greenham, R. H. Friend and D. D. C. Bradley, Angular Dependence of the Emission from a Conjugated Polymer Light-Emitting Diode: implications for efficiency calculations, *Adv. Mater.*, 1994, **6**, 491–494.

95 E. Yablonovitch, Statistical ray optics, *J. Opt. Soc. Am.*, 1982, **72**, 899.

96 *Surface Mount Led Red/Green, 0807 Package*, **https://www.bivar.com/parts_content/Datasheets/SM0807BC.pdf**.

97 Low-Power LEDs, *Neumüller Elektronik GmbH*, **https://www.neumueller.com/en/produktgruppe/low-power-leds**.

98 Ultra-Low Current LEDs, *DigiKey*, **https://www.digikey.com/en/product-highlight/s/sunled/ultra-low-current-leds**.

99 *Led Red Clear 2SMD*, **https://www.sunledusa.com/products/spec/XZCM2CRK53WA-8VF.pdf**.

100 W. T. Hadmojo, M. S. Qureshi and A. Nayfeh, Critical Roles of Nanoparticles in the Development of Perovskite Solar Cells: A Review, *Energy Fuels*, 2025, **39**, 7147–7166.